Una galaxia E+A al microscopio: Estudio detallado de SDSS J092006.43+015807.7 con MUSE

An E+A galaxy under the microscope: Detailed analysis of SDSS J092006.43+015807.7 with MUSE

Trabajo de Fin de Grado
Grado en Física
Universidad de La Laguna
Curso 2019/2020

Autora
Lucía Fernández Arroyo

Tutora
Ana Monreal Ibero

Contents

Resumen general

Las galaxias E+A fueron descubiertas por Dressler and Gunn en 1983. Estas se caracterizan por presentar flujos de absorción muy fuertes para las líneas de Balmer y también por la ausencia de [O II] en su espectro: en definitiva, no hay indicios de formación estelar en toda la estructura galáctica. Aunque se consideran un elemento clave en el estudio de la evolución galáctica, no existe mucha bibliografía sobre las E+A y tampoco está establecido el mecanismo mediante el cual se llegan a formar, aunque existen dos hipótesis: por interracción galaxia-galaxia o por "barrido por presión de arrastre" (ram-pressure stripping). En particular, para la galaxia que se estudia en este trabajo, SDSSJ092006.44+ 015807.7, la única información disponible en el óptico es una imagen en falso color y un espectro tomado en una apertura de 3" de diámetro de su región central.

El cubo de datos tomado por el espetrógrafo de campo integral MUSE (colocado en el VLT, Very Large Telescope) ha facilitado el estudio espectral de SDSS J092006.43+015807.7. Tras obtener los espectros observados para 22 regiones repartidas en toda la galaxia, se han pasado por el programa FADO para obtener la componente estelar modelada de los mismos. El espectro resultante de restar la parte estelar de la modelada (es decir, la componente del gas) se ha usado para medir los flujos integrados de varias líneas espectrales de las que hemos obtenido información a lo largo de todo el trabajo. Antes de poder interpretar los flujos, es necesario corregirlos de atenuación, que es el efecto que tiene el polvo interestelar sobre la luz que nos llega de un objeto. Para poder realizar esto, es imprescindible obtener el valor de atenuación de cada región. En este caso, se empleó el decremento de Balmer para la atenuación del gas y los resultados del modelado de FADO para la estelar. Por otra parte, se estudiaron diagramas de diagnóstico (BPT) para discernir el origen de la ionización del gas para cada apertura estudiada. También se ha estudiado la relación de las anchuras equivalentes del doblete Na D con la atenuación, así como la velocidad relativa de cada región respecto del núcleo galáctico.

La estructura del trabajo se divide en varios bloques. En primer lugar, se presenta una introducción a las galaxias E+A y a sus principales características espectrales, así como el instrumento usado (MUSE) para obtener el cubo de datos que se analizará en este proyecto. También se adjuntan algunos de los parámetros concretos para la galaxia que se va a estudiar, SDSS J092006.43+015807.7. En el segundo bloque se explica la metodología aplicada para la obtención de resultados: es decir, las líneas de trabajo que se han seguido, así como los programas usados. En particular, se resalta la creación de modelos para las líneas espectrales, clave para la derivación de los parámetros a discutir. Por último, se analizan los resultados, comparándolos con otros trabajos, ya sean sobre el mismo tipo de galaxia o de otras. Estos últimos se han usado para comparar valores de galaxias más estudiadas con lo que hemos obtenido para SDSS J092006.43+015807.7, y así resaltar el hecho de que las E+A son galaxias atípicas y de las que no se dispone tanta información. Cabe destacar que se ha incluido el estudio de un factor relacionado con la atenuación que, hasta donde sabemos, no se había plasmado anteriormente en un trabajo relacionado con las E+A.

Para finalizar el trabajo, realizamos una conclusión en la que se recopilan los principales resultados que hemos obtenido. La morfología de SDSS J092006.43+015807.7 y el tipo de rotación que presenta, indican que esta galaxia surgió de un merger entre dos galaxias con distinta masa. Además, el análisis de los diagramas de diagnóstico BPT apunta a que el núcleo está formado

por un AGN, cuya influencia podría ser la causante de la terminación de formación estelar. La gran cantidad de gas ionizado presente en la galaxia está fundamentada por los valores calculados para la atenuación tanto para el gas como para las estrellas y, además, el exceso de sodio es indicativo de que el contenido de medio interestelar también es alto, aparte del gas ionizado. Estos resultados son el fruto de un primer análisis de las características morfológicas y espectrales de SDSS J092006.43+015807.7. Hemos añadido, para cerrar el estudio, una serie de líneas de trabajo futuro que ayuden a afianzar lo que hemos concluido y que extiendan los conocimientos sobre esta galaxia y otras E+A.

List of Tables

List of Figures

Chapter 1

Introduction

Resumen. *En esta sección se presentan las galaxias E+A y se discuten los resultados más importantes de los estudios que se han hecho sobre este tipo de galaxias hasta la fecha. En particular, se describen sus características espectrales: fuerte absorción en las líneas de Balmer y ausencia de [O II] en el espectro. Esto implica que este tipo de galaxias ha sufrido un período de formación estelar que ha parado súbitamente, aunque el mecanismo por el cual se rige este proceso todavía no está determinado. También se explican algunos de los posibles orígenes de las E+A. A continuación, se muestra la información recopilada para la galaxia que se va a analizar (SDSS J092006.43+015807.7) y los datos que se van a usar en este trabajo. La información disponible incluye parámetros básicos (coordenadas, redshift,etc), una imagen en falso color y un espectro del núcleo (tomado de SDSS). Los datos espectrales de SDSS J092006.43+015807.7 se concentran en un cubo de datos de 240×220 píxeles (o 48"×44") tomado por MUSE, que es un espectrógrafo de campo integral colocado en el telescopio VLT UT4.*

1.1 E+A galaxies

Since their discovery by Dressler & Gunn (1983), E+A (also known as post-starbust) galaxies have been researched for their significance in the study of galaxy evolution. These galaxies are presumed to be a type of transition object within the well-known Hubble tunning fork. The acronym E+A reveals information straightaway about their morphology and stellar content: they are elliptical galaxies that show a distinctive population of A-type stars. These galaxies are also referred to as K+A because an important number of them present bulge-dominated, disturbed morphologies that are not associated with elliptical galaxies. E+A galaxies present strong Balmer absorption lines in their spectra, but no signs of [O II] emission lines whatsoever. Strong Balmer absorption lines are associated with A-type stars, which are main-sequence, blue-white stars with surface temperatures that range between 7600 and 10000 K. Due to the short life-span of this type of stars, the E+A evolutionary state is presumed to be very short, making them extremely rare (<1% of all galaxies in the local Universe) (Goto (2007)). [O II] emission lines are used to identify population of young, massive stars, as the UV radiation they emit is powerful enough to photo-ionize heavy elements, such as neutral oxygen. Its absence proves that there is no on-going star formation within the galaxy.

The origin of E+A galaxies is, to date, still discussed. The more plausible processes are ram-pressure stripping and galaxy interaction: ram-pressure stripping is associated with the movement of galaxies through the hot intracluster medium; galaxy interaction usually involves two colliding galaxies which ultimately may merge (Goto et al. (2008)). The ultimate quenching

of star formation is also a matter of study, but is has been proven that AGN-driven winds can strip a galaxy from its gas content (see Baron et al. (2018)). The way stellar populations (in particular, post-starbust regions) are distributed depends directly on the origin of the E+A galaxy: a galaxy interaction should result in a central, very condensed post-starburst region while gas stripping would create a much larger post-starburst region, which would be uniformly distributed within the galaxy (Goto et al. (2008)). A thorough mapping of the different stellar populations in the galaxy (using e.g. 2D spectroscopic information) is necessary in order to distinguish the origin of the post-starbust region. An E+A galaxy will be studied in this project, in particular SDSS J092006.43+015807.7.

1.2 Galaxy overview

SDSS J092006.43+015807.7 was part of an original sample of 2.5 million galaxies selected by an automatic classification algorithm (Baron & Poznanski (2017)). This galaxy has been barely observed and studied, and the only available information in the optical is provided by the SLOAN Digital Sky Survey (SDSS) (Aguado et al. (2018))[1]. The aim of SDSS is the creation of the most detailed three-dimensional map of the Universe, both with multi-color images and spectra of millions of astronomical objects. This data is collected in Table 1.1.

Parameter	Value	Ref.
Name	SDSS J092006.43+015807.7	
RA (J2000.0)	9h20m6.4s	(a), (c)
Dec(J2000.0)	1d58m7.7s	(a), (c)
z	0.08498	(a), (f)
D (Mpc)	380.6	(b)
scale (pc/")	1812	(b)
radial velocity (km/s)	25482.622	(a), (f)
$A_{\lambda,gal}$ (V)	0.068	(b), (g)
G	18.649	(a), (c)
J	13.822	(a), (d)
H	13.205	(a), (d)
K	12.610	(a), (d)
u	18.773	(a), (e)
g	16.743	(a), (e)
r	15.774	(a), (e)
i	15.295	(a), (e)

Table 1.1: Basic data for SDSS J092006.43+015807.7. **References:** (a) SIMBAD Astronomical Database; (b) NASA/IPAC Extragalactic Database (NED); (c) Gaia Collaboration (2018); (d) Skrutskie et al. (2006); (e) Ahn et al. (2012); (f) Ahn & et al. (2013); (g) Schlafly & Finkbeiner (2011)

The SLOAN survey also provides a false-colour image (Figure 1.1 (a)) and a 3" diameter spectrum of its nucleus (Figure 1.1 (b)), which according to the scale provided in Table 1.1, represents a 5.436 kpc-wide region of the galaxy. The SLOAN Survey provides spectra with relatively low spectral resolution ($R_{min} = 1500$ at $\lambda = 380$ nm and $R_{max} = 2500$ for $\lambda = 930$ nm) but for this particular galaxy it is enough to initiate a first approach to its spectroscopic features.

[1] `https://www.sdss.org/`

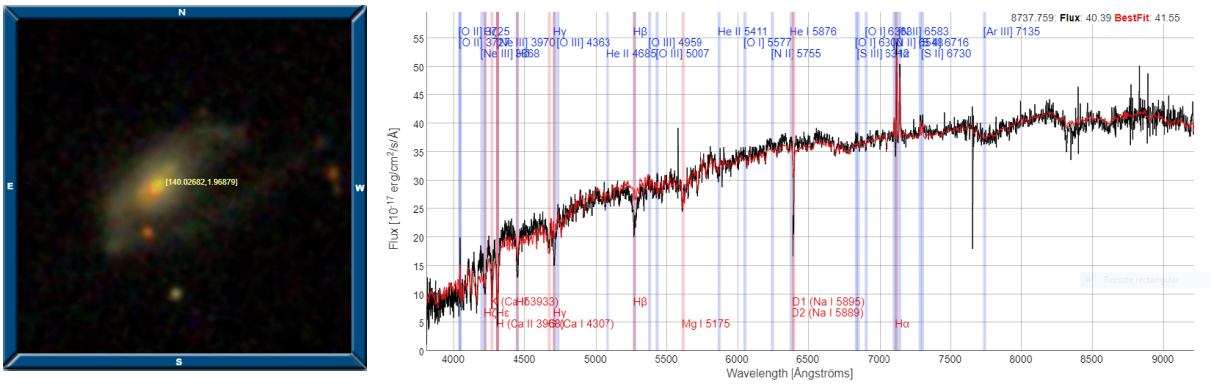

(a) (b)

Figure 1.1: (a) False colour image of SDSS J092006.43+015807.7. *Image credits:* SciServer; (b) SDSS spectrum *Image credits:* SDSS Science Archive Serve (SAS). In (b), the black spectrum consists of the SLOAN spectrum of the 3" diameter region of the nucleus. The red spectrum is generated by the automatic SLOAN modelling code. Both absorption (red vertical lines) and emission lines (blue vertical lines) are depicted in the image. It is clear that absorption in Hβ is especially strong and the SLOAN modelling does not fit this component. This was the initial indication that implied that we would need to add an extra component in order to study the integrated flux of Hβ.

In Figure 1.1 (b) it is notable that the spectrum is reddened; that is, the intensity of the flux increases towards longer wavelengths. The light that is observed from a galaxy (particularly, the continuum and the absorption lines) is a combination of the spectra emitted by the stars, and it is reddened by the dust present in the interstellar medium (ISM) within the galaxy and along the line-of-sight. A-type stars have a relatively blue spectrum, so the dust's influence on the spectrum seems significant. Also, [O II] is relatively faint in Figure 1.1(b). The data used for this work does not contain the spectral range that includes [O II]. Thus, it will not be addressed here.

1.3 Integral Field Spectroscopy and the MUSE

Integral Field Spectroscopy (IFS) is an observing technique which allows to obtain the electromagnetic spectrum for each pixel position in a telescope image over a continuous area on the sky. A data cube is obtained, usually in the FITS format. A schematic depiction of a data cube is presented in Figure 1.2 (a). The examined spectral data for SDSS J092006.43+015807.7 was obtained with MUSE, which is an integral field spectrograph installed in the VLT UT4 telescope (see Figure 1.2 (b)). This instrument generates a spectrum for each pixel or cell of an image of an extended object, such as a galaxy. The instrument presents an 1×1 arcmin field of view and a spatial sampling of 0.2"/pixel. The spectral resolution of MUSE, which works on the visible portion of the electromagnetic spectrum, varies with the observed wavelenght, λ: $R_{min} = 1750$ for $\lambda = 465nm$ and $R_{max} = 3750$ for $\lambda = 930nm$.

This work has been done using a cropped version of the final processed data cube (that is, reduced, calibrated in flux and wavelength, and corrected for galactic extinction) around the studied galaxy. The processing was done using the public MUSE Instrument Pipeline v1.6.1 (Weilbacher et al. (2020)) and prior to the beginning of this work. The resulting cube has a

dimension of 240 × 220 pixels, or 48” × 44”. According to the scale provided in Table 1.1, the mapped area is equivalent to ∼ 87 × 79 kpc.

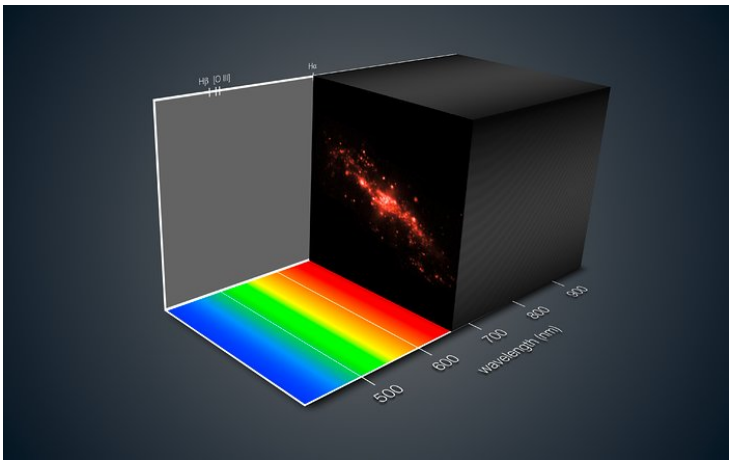

(a)

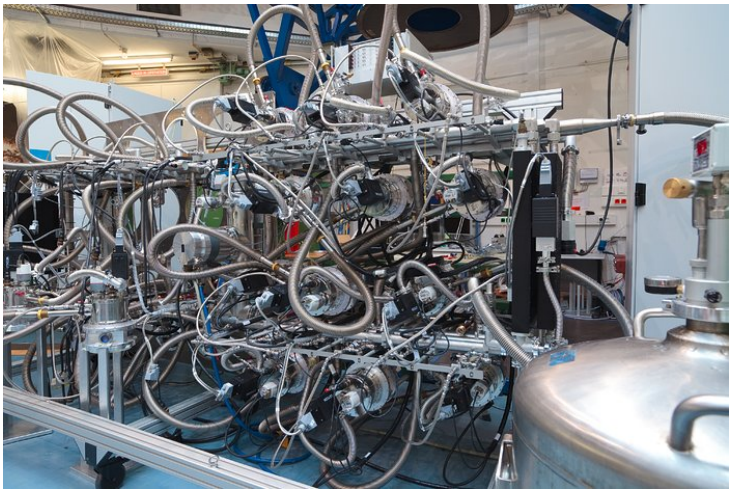

(b)

Figure 1.2: (a) Data cube obtained using IFS, (b) MUSE. *Image credits:* (a) and (b) European Southern Observatory (ESO)

Chapter 2

Objectives

Resumen. *El objetivo de este Trabajo de Fin de Grado es establecer un primer análisis de los datos de MUSE para la galaxia E+A conocida como SDSS J092006.43+015807.7. Nuestro propósito es comprender y establecer el estatus de SDSS J092006.43+015807.7 como galaxia E+A, a la vez que intentar mejorar y ampliar nuestro conocimiento acerca de estas escurridizas galaxias. Esto requiere un estudio integral y combinado de todos las componentes de la galaxia; esto es, el gas (tanto neutro como ionizado), el polvo, las poblaciones estelares, y la posible presencia de un núcleo galáctico activo (AGN, siglas en inglés). En esta memoria nos centraremos en el análisis del gas y el polvo, y proponemos las componentes restantes como interés de estudio para trabajos futuros. El enfoque de este estudio está enmarcado dentro de las limitaciones computacionales que se han manifestado por el uso del portátil de la autora. Debido a esto, enfatizaremos la comprensión de los conceptos teóricos en los que se basa todo el trabajo, así como en las herramientas empleadas para la derivación los parámetros de estudio.*

The objective of this work is to establish a first approach in the analysis of the MUSE data for the E+A galaxy known as SDSS J092006.43+015807.7. Our purpose is to understand and establish SDSS J092006.43+015807.7's status as an E+A galaxy, whilst improving and extending our knowledge of this elusive galaxies. This requires a comprehensive and ensembled analysis of all the components of the galaxy: gas (both neutral and ionized), dust, stellar populations, and a putative Active Galactic Nucleus (AGN). In this work, we will focus on the study of gas and dust, leaving the other components as a central topic for future works. The extent of the study is framed within the computational limitations encountered when using the author's laptop. Because of this, we will put emphasis on the understanding of the theoretical concepts that we based the analysis on, and on the tools employed to derive the studied parameters.

Chapter 3

Methodology

Resumen. *Para el estudio de las características espectrales de SDSS J092006.43+015807.7 se han escogido 22 aperturas de 0.5 arcsec de diametro, distribuidas por toda la estructura galáctica. Los correspondientes espectros se han extraido, analizado y modelado con FADO y con una serie de scripts en python de desarrollo propio. De esta forma, se han obtenido los flujos integrados para varias líneas espectrales (en concreto Hβ, [O III]λλ4959,5007, [N II]λλ6548, 84, Hα and [S II]λλ6716, 31) y las anchuras equivalentes del doblete Na D en absorción. En esta sección se explica la metodología usada para obtener los datos mencionados anteriormente, así como los parámetros que se han calculado y los diagramas que se han construido a partir de los mismos: la atenuación, los diagramas BPT y la velocidad relativa para las distintas regiones.*

3.1 Regions and spectra

As an initial approach to this work, we selected some interesting regions of the galaxy in order to study their respective spectra. Computational limitations restricted the number of regions, so a complete mapping of SDSS J092006.43+015807.7 was not done. However, the most prominent areas of the galaxy are well depicted within the limitations; that is, its nucleus and both tidal tails (see Section 4.1). The result is a sample of 22 regions of circular aperture, with a diameter of 0.5 arcsec (2.5 image pixels, or spaxels) which were selected using ds9[1] (see Figure 3.1). With the selected diameter, the sum of 6.25 spaxels is being studied and that improves the S/N ratio in a factor of ∼2.5, compared to that provided by a single spaxel.

The spectrum for each region was extracted using the MUSE Python Data Analysis Framework (MPDAF). This Python package provides tools to work with MUSE specific data and more general data like spectra, images and data cubes [2].

[1] `https://sites.google.com/cfa.harvard.edu/saoimageds9`
[2] `https://mpdaf.readthedocs.io/en/latest/`

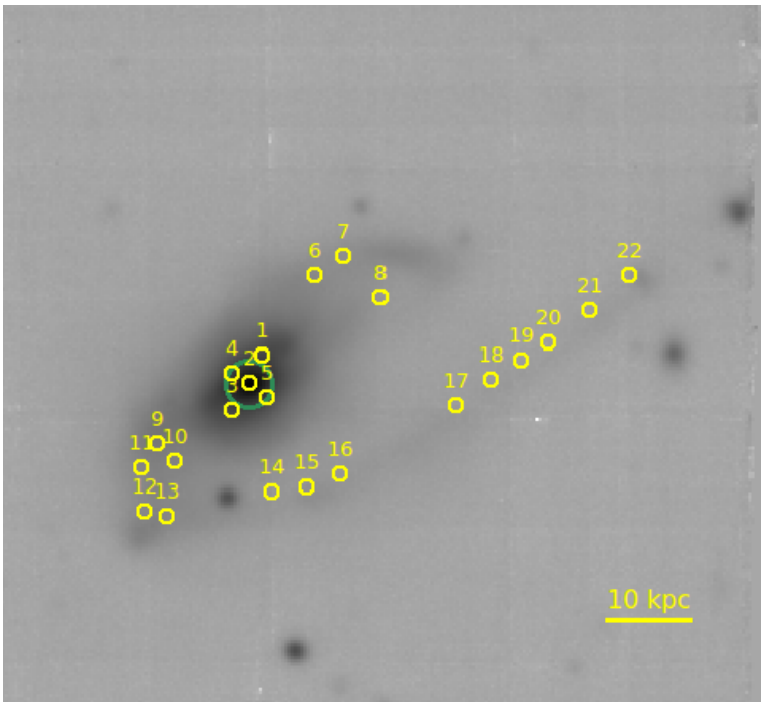

Figure 3.1: The 22 circular, 0.5" diameter apertures that were selected for this work. A scale of 10 kpc is added in order to guide the reader. The larger aperture represents the 3" diameter region of the SLOAN spectrum shown in Figure 1.1. The image corresponds to the integrated flux of Hα and its continuum in narrow filters, in a logarithmic scale.

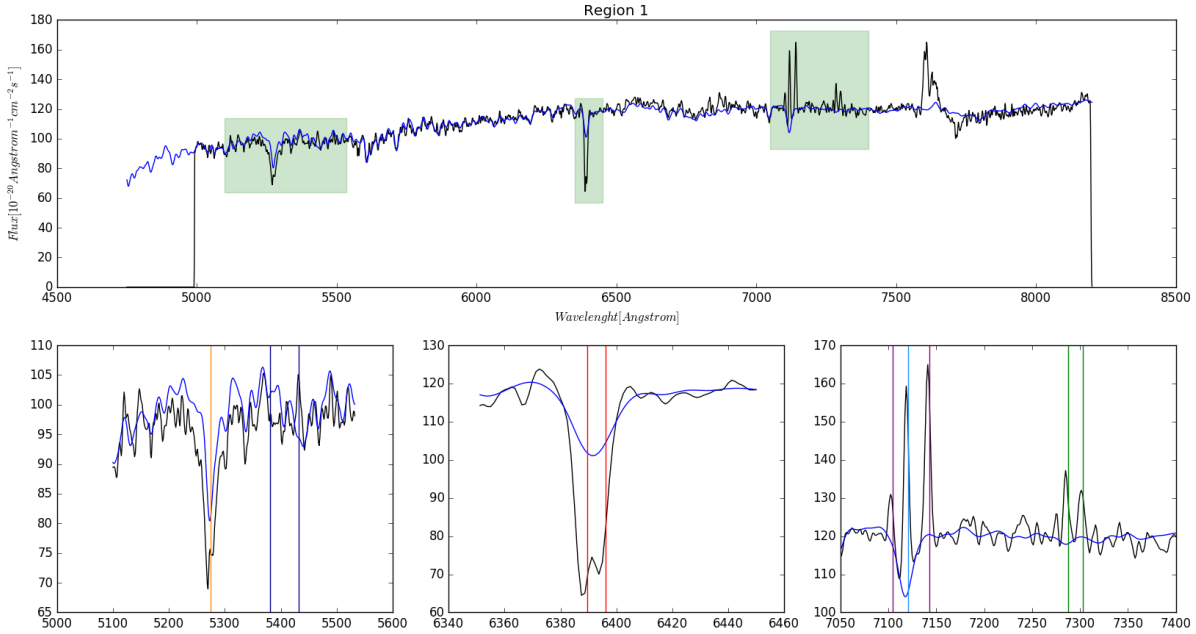

Figure 3.2: First spectral analysis of Region 1. The black spectrum represents the observed spectrum and the blue one the model created by FADO. The vertical, coloured lines mark the rest-frame central wavelength of the studied spectral lines, based on the redshift provided in Table 1.1. The three smaller plots are centered in the studied spectral lines: (from left to right) i) Hβ (orange vertical line) and [O III]$\lambda\lambda$4959, 5006 (dark-blue vertical lines) ii) Na$\lambda\lambda$5889, 95 and iii) Hα (light blue vertical line), [N II]$\lambda\lambda$6548, 83 (purple vertical lines) and [S II]$\lambda\lambda$6716, 31 (green vertical lines).

A representative spectrum of one of the 22 regions is shown in Figure 3.2 (in particular, for Region 1, located at the nucleus). The contribution of the stellar emission and the gas has not been separated for this example; that is, it shows the observed spectrum as it was extracted (black spectrum in the aforementioned figure). This step will be explained in Section 3.2. In addition, in that same section, it will be explained how we obtained the stellar spectra for each region using FADO (Fitting Analysis using Differential evolution Optimization). In Figure 3.2, the blue spectrum corresponds to the modelled overall spectrum that is also provided by FADO.

The three smaller spectra that are plotted correspond to the particular regions of the spectrum that will be studied in this work, and they match the highlighted rectangles in the main graph. It is notable that the initial modelling by FADO for the lines was satisfactory in most of the spectral range, with the exception of some specific windows. This will be addressed later in this work, particularly in Section 3.3.

The spectral resolution for this example is larger than the spectrum seen in Figure 1.1 (b), as it corresponds to data obtained by MUSE, not the SDSS.

3.2 Subtraction of stellar emission

Population spectral synthesis's goal is to solve the mass, age and metallicity of a galaxy's stellar populations using its spectrum. It has been widely used in the study of galaxy assembly history of large spectroscopic data sets, in particular SDSS. FADO (Fitting Analysis using Differential evolution Optimization) is the population synthesis code used in this work in order to obtain information for both the stellar and nebular emission fits. It consists of a novel code that models the sum spectrum (affected by a particular attenuation and redshift) from a linear relation between simpler stellar populations' spectra. The aim is to accurately reproduce a given observed spectrum. FADO's performance can be described in three main steps: 1) pre-processing of spectral data, 2) spectral synthesis through genetic DEO (Differential Evolution Optimization) and 3) computation and storage of the model output. These stages are extensively described in Gomes & Papaderos (2017), as well as the mathematical foundation. From a given spectral input, it ultimately gives a series of FITS files, which contain information regarding the modelled spectrum and other stellar and spectral parameters.

The spectra obtained in Section 3.1 were run through FADO in order to obtain the best-fitting synthetic SED (Spectral Energy Distribution) and other wavelength-dependent quantities, particularly the best-fitting stellar component of the spectrum. Other parameters were also used and taken from the different FITS files that FADO provides as an output and will be discussed latter in this work. Unfortunately, FADO could not adequately model the fluxes for some of the lines, specifically $H\beta$ (see Appendix A). A first approach to this issue was to run FADO using masks for the problematic lines. However, the results were not fully satisfactory, so we neglected the usage of masks.

Once every individual observed spectrum was run through FADO, we had to resample the results to MUSE's standards, so both observed and modeled spectra could be compared: the wavelength step-size for the FADO output was 1.1Å, which is different to MUSE's dispersion, which is 1.25Å. This was done in order to derive the gas component of the observed spectra, since the original data contains information for both the stellar and gas contributions. The resampling of FADO's output was necessary to subtract the stellar modelled spectra from the observed data,

thus obtaining the gas component:

$$O_\lambda - S_\lambda = G_\lambda \tag{3.1}$$

where O_λ stands for the observed spectrum, and S_λ and G_λ represent the components for the stars and gas, respectively.The interest of this process is the measurement of the integrated fluxes of some compelling emission lines, particularly $H\beta$, $H\alpha$, and the [O III]$\lambda\lambda$4957, 5007, [N II]$\lambda\lambda$6548, 83 and [S II]$\lambda\lambda$6716, 31 doublets. The first two lines are necessary for the study of dust attenuation and the ultimate de-reddening of all the other ones (see Section 4.2). The doublets are required to study the ionization mechanisms operating in the galaxy by means of well-known diagnostic diagrams (see Section 4.4). Finally, we used the central wavelength of Hα in order to estimate gas velocities and the type of rotation present in the galaxy.

3.3 Emission-line fluxes

The emission lines from the gas spectra obtained in Section 3.2 were fitted to a Gaussian model (taking into account the shape of the continuum) using the suitable astropy[3] (Astropy Collaboration et al. (2013); Price-Whelan et al. (2018)) functions and then integrated in flux. This was done for all regions and for every spectral line and doublet, and implementing the standard constraints. Nonetheless, the errors for the resulting model were not provided, so we applied the following estimation for each emission-line flux, which is presented in Castellanos et al. (2002):

$$\sigma_{line} = \sigma_{cont} \times N^{1/2} \left(1 + \frac{EW}{N\Delta\lambda}\right)^{1/2} \tag{3.2}$$

where σ_{cont} is the standard deviation in the continuum close to the line of interest, N is the number of pixels sampling the line, EW is its Equivalent Width and $\Delta\lambda$ is the dispersion in Å pixel^{-1} (for MUSE data, this value is 1.25 Å pixel^{-1}). For EWs below 3 Å, the corresponding term in Equation (3.2) could be disregarded because the value for N is much more prominent. Since the studied EWs were typicaly below the previous limit, the corresponding term in Equation (3.2) was neglected.

The model for Hβ was the most challenging one to achieve. We had to add an extra component in order to compensate for the strong absorption (more details on this in Section 4.3), yet the model was not as satisfactory as for the other lines. An example of this particular behaviour is shown in Figure 3.3. However, it was possible to obtain preliminary results for the galaxy under study, which will be discussed in Section 4.

[3] https://www.astropy.org/

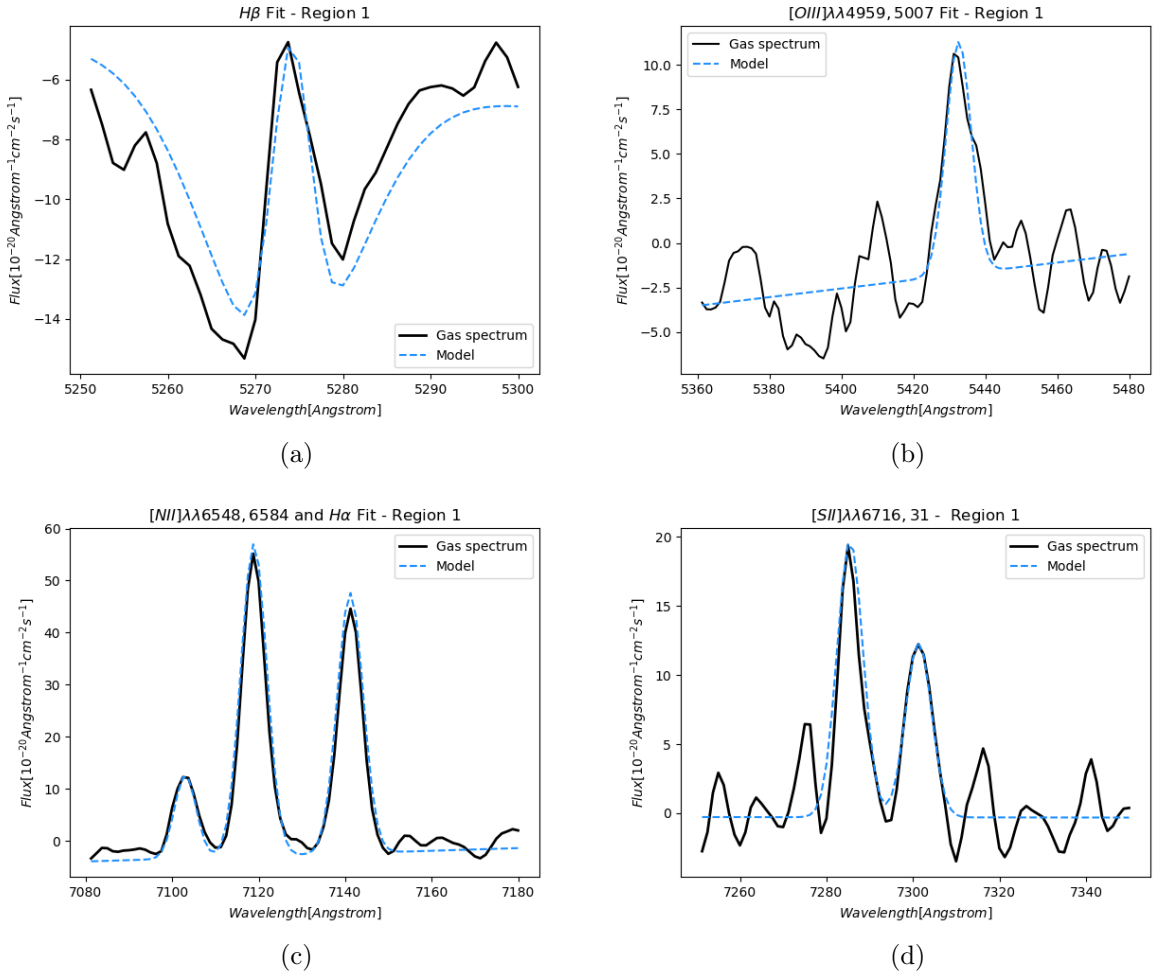

Figure 3.3: Models created for the spectral lines in Region 1. The black spectra represents the observed spectrum after removal of the stellar emission modeled by FADO. The blue dashed line is the model. (a) Hβ, (b) [O III]$\lambda\lambda$4959,5007 (for this particular region, only [O III]λ5007 could be measured), (c) Hα and [N II]$\lambda\lambda$6548, 6584, and (d) [S II]λ6716, 31.

3.4 The Sodium absorption doublet

The Na$\lambda\lambda$5889, 95 doublet (or Na D) was also studied but it had to be treated differently. The absorption doublet was also fit into a Gaussian model (see Figure 4.4), but the EWs were measured, instead of the integrated flux. The EW corresponds to the width of the adjacent continuum of a spectral line that has the same area as the absorption line. This value is independent of the shape of the line and it is defined as:

$$EW_\lambda = \int \frac{F_0 - F_\lambda}{F_0} d\lambda = \int (1 - \frac{F_\lambda}{F_0}) d\lambda \tag{3.3}$$

where F_0 is the continuum intensity on either side of the absorption line and F_λ is the intensity of the wavelenght of interest. Typically, the limits of the integral are set for two wavelengths, λ_1 and λ_2, close to the central λ of the studied line. A diagram that illustrates this definition is represented in Figure 3.4.

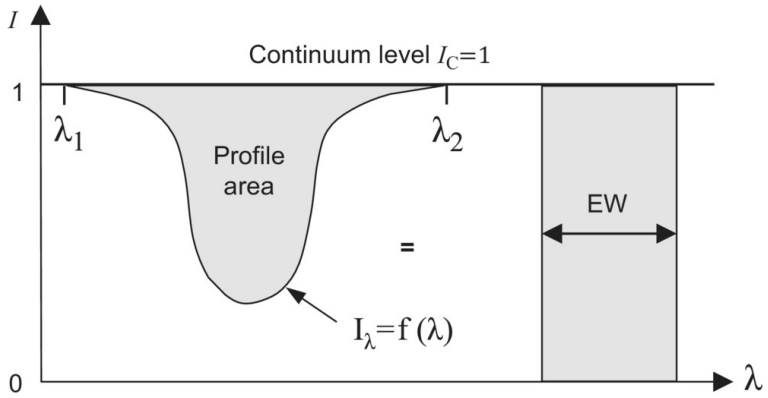

Figure 3.4: Definition of equivalent width. The nomenclature in this image is slightly different to the one we used for our definition: $I_c = 1$ corresponds to the normalised continuum intensity and $I_\lambda = F$. *Image credits*: Cambridge University Press.

For this procedure, we used the resulting O_λ/S_λ spectra, which by construction has a normalized continuum (see Figure 4.4). Measuring the flux is equivalent to measuring the EW in this case, and the uncertainty for this was calculated using Equation 3.2.

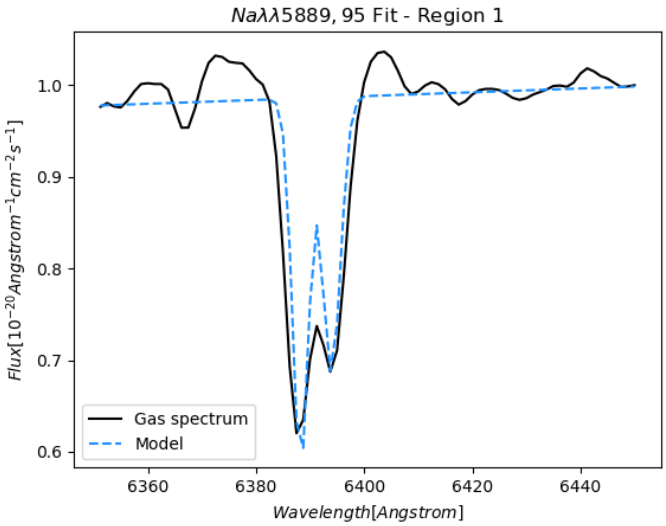

Figure 3.5: Model for the Na$\lambda\lambda$5889, 95 doublet.

Several possibilities can explain the excess in the Na D lines. They could be due to the presence of rare stars, e.g. T-tauri stars (see Pascucci et al. (2015)), but this hypothesis is not plausible and we will not dwell on it. Also, it can be associated to abnormal stars, with higher than expected relative Na abundances. However, FADO already takes into account the stellar Na D (at least to some extent), and the red spectrum displayed in Figure 1.1 indicates that the observed excess observed is rather notable suggesting an interstellar origin as the most plausible one. This is the adopted hypothesis in this work.

3.5 Extinction and dust attenuation

The electromagnetic spectrum that is acquired from a galaxy does not only provide information about its stellar population: dust and gas also influence the observed emission and absorption component of the spectrum. These can be homogenous or heterogenously mixed with the stars, depending on the region of the galaxy and its morphology and structural composition. When they are uniformly distributed within a group of stars the fluxes of emission lines are slightly attenuated; however, when a dusty, gas surrounds them, the dust acts as an opaque-like screen and the consequences on the overall spectrum are greater. In both cases, the received light appears reddened, and more so towards the UV part of the spectrum. This effect is called dust attenuation and it indicates the absorption and scattering by dust grains into the observer's line of sight. It is sometimes referred as interstellar extinction[4]. Since the influence of dust attenuation is not negligible it must be corrected when studying any type of galaxy. An exemplary explanation of this is found in Osterbrock & Ferland (2005). Dust reduces the amount of light from a source emitting through the interstellar medium (ISM) according to the following equation:

$$I_\lambda = I_{\lambda 0} e^{-\tau_\lambda} \tag{3.4}$$

where $I_{\lambda 0}$ is the intensity that would be received in the absence of attenuation along the line of sight, I_λ is the intensity actually received, and τ_λ the optical depth for a given wavelength. In the optical region (which is the region of the spectrum that will be studied in this work), it has been found that $\tau_\lambda = Cf(\lambda)$, where the constant value C depends on the line-of-sight and the function $f(\lambda)$ describes the relative absorption for each wavelength. This is assumed to be the same for all line-of-sights. This implies that the physical properties of the dust are similar all around the same area of space.[5] It has been revealed that attenuation differs greatly among stars in the UV spectral region, especially at the shortest measured wavelengths, but this is not a spectral range considered in this work.

The ratio of observed intensities of two emission lines is also affected by attenuation:

$$\frac{I_{\lambda 1}}{I_{\lambda 2}} = \frac{I_{\lambda 1,0}}{I_{\lambda 2,0}} e^{-(\tau_{\lambda 1} - \tau_{\lambda 2})} \tag{3.5}$$

If we assume the average form for attenuation, Equation (3.5) can also be written as:

$$\frac{I_{\lambda 1}}{I_{\lambda 2}} = \frac{I_{\lambda 1,0}}{I_{\lambda 2,0}} e^{-C[f(\lambda 1) - f(\lambda 2)]} \tag{3.6}$$

The correction for the ratio of intensities will only depend on the form of the attenuation curve ($f(\lambda)$) and on the amount of extinction. The principle to determine the amount of correction is to use the intrinsic intensity ratios of two emission lines so in Equation (3.6) only C is unknown. Once the equation is solved for said factor C, the average reddening curve at all wavelengths can be calculated and used to correct different emission-line ratios.

One method frequently used to determine dust attenuation is the measurement of the ratios of two or more HI Balmer lines; particularly for this work, the Balmer decrement (that is $H\alpha/H\beta$) will be used. Both lines are produced by the ionization of gas by young stars, so it provides

[4] Attenuation must not be mistaken for extinction, as the latter indicates the absorption and scattering by dust grains *out* of the observer's line of sight. These terms are erroneously interchanged.

[5] Even though this is a good approximation, in-depth observations reveal variations in the $f(\lambda)$ along different light paths in a galaxy.

a good quantification of the dust attenuation due to birth clouds (BCs), where dust is highly concentrated. Colour excess is proportional to dust attenuation (A_V from now on) and for the Balmer decrement method it is calculated using the equation from Osterbrock & Ferland (2005):

$$E(B-V) = 1.97 log_{10}\left[\frac{(H\alpha/H\beta)_{obs}}{2.87}\right] \tag{3.7}$$

Equation (3.7) assumes an intrinsic value of the Balmer decrement $(H\alpha/H\beta)_{int} = 2.87$. The conditions for which this number is valid follow the Case B recombination conditions (Osterbrock & Ferland (2005))[6]. Attenuation can also be estimated using stellar population modelling. In particular, we used FADO in order to work out $A_{V,stel}$ for all regions.Regarding the shape of the attenuation curve, we used the Galactic average extinction law. This is characterized by the following total-to-relative attenuation $R_V = A_V/E(B-V) = 3.1$ (Rieke & Lebofsky (1985)). Attenuation in each region can then be calculated using the relation $A_{V,gas} = R_V E(B-V)$. The results will be discussed and compared to values reported for other type of galaxies in Section 4.2.

Once all the attenuations were determined, the next step was to correct the emission-line fluxes from interstellar reddening and it was done using PyNeb [7](Luridiana et al. (2015)), the 'CCM89' extinction law (Cardelli et al. (1989)). The extinction corrected relative fluxes will be discussed in Section 4.3.

3.6 BPT Diagrams

Baldwin et al. (1981) suggested a set of three diagnostic diagrams to determine the main energy source in emission-line galaxies. These diagrams are known as Baldwin–Phillips–Terlevich (BPT) diagrams and are based on the following optical line ratios $[O\,\text{III}]5007\lambda/H\beta$, $[N\,\text{II}]6584/H\alpha$, $[S\,\text{II}]\lambda\lambda 6716,31/H\alpha$, and $[O\,\text{I}]/H\alpha$. Eventually, the charts allow an identification among the following energy sources: HII regions (star-forming galaxies), Active Galactic Nucleus, Seyfert and Low-Ionization Nuclear Emission-line Region (LINER). However, additional mechanisms (e.g. shocks, post-AGB stars, etc) can explain the origin of the line ratios that are presented in BPT diagrams. The theoretical limits that rule the classification can be found in Kewley et al. (2006) and will be used in this work to create an introductory categorization of the ionization mechanism SDSS J092006.43+015807.7.

For this work, the diagrams were created with the $[O\,\text{III}]\lambda 5007/H\beta$, $[N\,\text{II}]\lambda 6584/H\alpha$, and $[S\,\text{II}]\lambda\lambda 6716,31/H\alpha$ ratios. This was done for all regions where the corresponding fluxes could be measured. A comparison between the values obtained for the corrected and non-corrected fluxes will be discussed in Section 4.4.

3.7 Relative velocities

The Doppler effect is used in astronomy in order to determine if an object is approaching or receding from the viewer. This phenomenon can be seen in flux versus wavelength spectra: if the spectral lines are displaced towards the blue part of the spectrum, the object is approaching; if they are displaced towards the read, it indicates that the object is receding. In this work, we used the gas component of the observed spectra determined in Section 3.2 to calculate the

[6]Electron temperature of $T_e = 10^4 K$ and electron density of $n_e = 100 cm^{-3}$.
[7]`http://research.iac.es/proyecto/PyNeb//`

velocities at which the different apertures are moving.

The Hα emission line was the spectral feature that we were able to measure for almost all the selected apertures. We used this line to obtain the gas velocity for each region with the following equation:

$$v_{H\alpha} = \frac{\lambda_{obs} - \lambda}{\lambda_{obs}} \times c \tag{3.8}$$

where λ_{obs} is the observed central wavelength, λ is the assumed value for Hα, c is the speed of light in km s^{-1}. Then the central velocity (that is, the one for the nucleus) was subtracted to the different results to obtain the relative values to that aperture. We considered the central velocity to be the one calculated for Region 2 (see Figure 3.1), which was 25564 km s^{-1}. On another note, regarding the stars, we simply adopted the velocities determined by FADO. The relative velocities will be discussed in Section 4.6.

Chapter 4

Results

Resumen. *A continuación se presentan los resultados obtenidos a partir del análisis de las características espectrales de SDSS J092006.43+015807.7 en el óptico. En primer lugar se analiza la morfología de la galaxia, en particular las colas de marea. A continuación se detallan los resultados obtenidos para la atenuación del gas y las estrellas, y se realiza una comparación con trabajos centrados en otro tipo de galaxias. Cabe destacar que en este apartado se realiza el estudio de un parámetro (que relaciona ambas atenuaciones) del que no tenemos constancia que se haya publicado, hasta la fecha, un estudio en el que se analice. A partir de los valores de atenuación calculados para el gas se han corregido los flujos integrados relativos de las líneas espectrales que, a su vez, se hemos usado para estudiar los mecanismos de ionización presentes en la galaxia. Por otra parte, hemos comprobado que para esta E+A en particular, el doblete de sodio no traza la atenuación del gas y, para finalizar, realizamos un breve análisis sobre la rotación del mismo.*

4.1 Overall morphology

SDSS J092006.43+015807.7 exhibits a bulge-dominated, disturbed morphology; that is, at least two tidal tails are perceivable (see Figure 1.1 (a)). These are located at both sides of the galaxy. The smaller one (regions 6 to 8, both included) presents a size of roughly 21 kpc and is located to the north-west of the nucleus (see Figure 1.1); the other one (regions from 9 to 22, both included) is much larger, with an apparent size of 75 kpc and is located to the south and west of the nucleus. One of the mechanisms that triggers star formation is the interaction between two galaxies which ultimately results in a merger. Furthermore, it has been observed by Goto (2005) that a high percentage of E+As show tidal features. It is discussed in the same work that some of this galaxies present a satellite galaxy or are themselves one, and overall, the galaxy interaction theory seems to be much more established than the ram-pressure stripping one. Also, Goto et al. (2008) concluded that a galaxy-galaxy interaction (albeit with equal mass) can create a uniformly distributed post-starbust region throughout the E+A. We can establish, then, that the galaxy selected for this work presents a morphology that is similar to other post-starbust galaxies. The overall morphology of this particular galaxy suggests that it is the outcome of a merger of (at least) two galaxies.

4.2 Gas and stellar attenuation

Gas and stellar attenuation values were determined as explained in Section 3.5. These results are collected in Table 4.1, and it is notable that attenuation is high for both types: gas attenuation

($A_{V,gas}$) reaches values of 4.64 and stellar attenuation ($A_{V,stel}$) maximum value is 3.24. Such large values indicate that there is a considerable amount of dust within the galaxy. Additionally, this supports our hypothesis of interstellar origin for the sodium excess (see Section 3.4).

Region	$A_{V,gas}$	$A_{V,stel}$	Region	$A_{V,gas}$	$A_{V,stel}$
1	2.54 ± 0.03	0.92	13	2.07 ± 0.25	0.39
2	4.64 ± 0.03	2.13	14	2.19 ± 0.30	0.74
3	3.00 ± 0.02	3.24	15	1.95 ± 0.21	0.03
4	2.16 ± 0.03	0.78	16	2.15 ± 0.28	0.64
5	1.90 ± 0.04	0.50	17	2.54 ± 0.42	1.76
6	2.33 ± 0.21	0.31	18	2.14 ± 0.28	0.61
7	2.09 ± 0.26	0.44	19	2.57 ± 0.43	1.85
8	2.21 ± 0.30	0.80	20	2.70 ± 0.47	2.23
9	1.98 ± 0.34	0.13	21	2.21 ± 0.30	0.81
10	2.04 ± 0.24	0.30	22	2.95 ± 0.56	2.97
11	2.04 ± 0.24	0.29			
12	2.11 ± 0.27	0.52			

Table 4.1: Attenuation values for the gas and the stellar population. Values in blue were determined using a first degree polynomial fit.

Some values for the gas attenuation could not be determined using Equation (3.7), particularly for the apertures located in the tidal tails. In those regions, the flux for Hβ could not be measured. A first degree polynomial fit was done for four of the internal regions in order to have a first estimation of $A_{V,gas}$ (see Figure 4.1) in those apertures where the gas attenuation could not be determined using the Balmer decrement. The errors for the $A_{V,gas}$ values in black (see Table 4.1) were estimated by propagation of errors and those in blue were calculated the same way but taking into account the covariance matrix given by the polynomial fit. $A_{V,stel}$ values were all taken from FADO's output when running the code on the spectra. These values will be used to make the subsequent corrections of the relative emission fluxes (see Section 4.3) that enabled us to evaluate the ionization mechanisms in the galaxy. However, the aproximated attenuation values should be confirmed with integrated fluxes calculated from bigger apertures, improving the S/N ratio.

From Table 4.1 and Figure 4.2 it is noticeable that higher attenuation values (both for gas and stars) are found in the nuclear region of the galaxy, although some strong values can also be found in the larger tidal tail. However, there is not a relevant pattern which dictates how this values are distributed, other than the high values in the nucleus.

The study of the distribution of attenuation within E+A galaxies is not prominent yet, but it is interesting to compare the results that we found with those applicable for other types of galaxies. For example, for spirals, it has been determined by several studies (e. g. Greener et al. (2020)) that $A_{V,gas}$ and $A_{V,stel}$ both decrease with galactocentric radius. Clearly, the galaxy studied in this work is not a spiral one, yet the comparison between diverse studies on attenuation is enticing. Nonetheless, it is interesting to note that not only E+A galaxies present characteristic spectral features, but also (presumably) peculiar attenuation distributions.

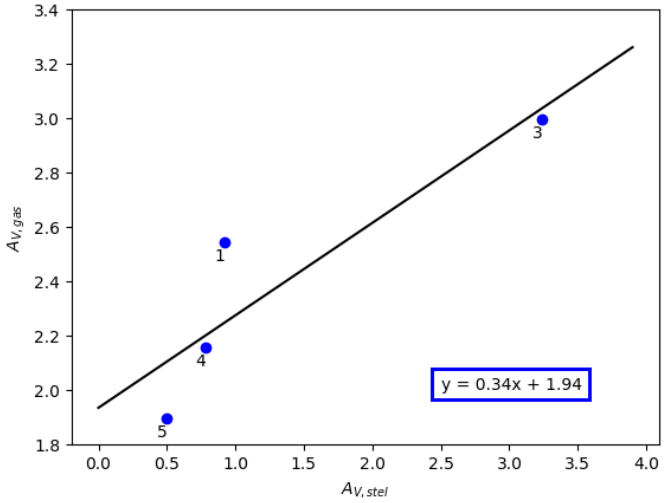

Figure 4.1: First degree polynomial fit for attenuation. The regions used correspond to the nucleus. The data for region 2 was not used because it was too high, both for the gas and stellar attenuation, and it was not properly fit.

On another note, attenuation values are much higher for the gas ($A_{V,gas}$) than for the stars ($A_{V,stel}$). This is representative for galaxies where star formation is taking place. In this regions, young stars have not yet detached from the circumstellar dust shell and it acts as a "screen" that enhances attenuation. The analysis of Table 4.1 suggests that attenuation values (both for the gas and the stars) are higher for the internal regions and that the ionized gas (regardless of the ionization source) is found behind or buried in zones with higher dust abundance. The stellar population also presents attenuation, but these are located where ISM is more diffuse. All in all, given the values that we calculated, we conclude that the most-recently formed stars could still be embedded still in their molecular birth clouds.

It has been found by Calzetti et al. (2000) that the relation between the global ratio of reddening, $E(B-V)$, affecting the stellar continuum to that derived from the Balmer decrement was equal to 0.44 ± 0.03 for star-forming galaxies. This value for spiral galaxies has been studied by Greener et al. (2020) and a value of $A_{V,stel}/A_{V,gas} = 0.57 \pm 0.04$ was found. In this work, it is also stated that the ratio does not vary significantly between the nucleus and the outer parts of spiral galaxies. We found that the ratio for the studied galaxy is $(A_{V,stel}/A_{V,gas})_{gal} = 0.517 \pm 0.328$. This is similar to what has been calculated for spiral and star-forming galaxies, even though they are clearly different kind of objects. To our knowledge, these are the first spatially resolved measurements of the attenuation values and their distribution in an E+A galaxy. In order to determine the value of this ratio for other parts of the galaxy (that is, the tidal tails), it is necessary to obtain an improved S/N ratio for those regions (e.g. using larger apertures). A possible future line of work would be to determine if the $A_{V,stel}/A_{V,gas}$ remains constant for all the galactic structure (as in spirals, and as we have assumed in lack of other information) or if it varies.

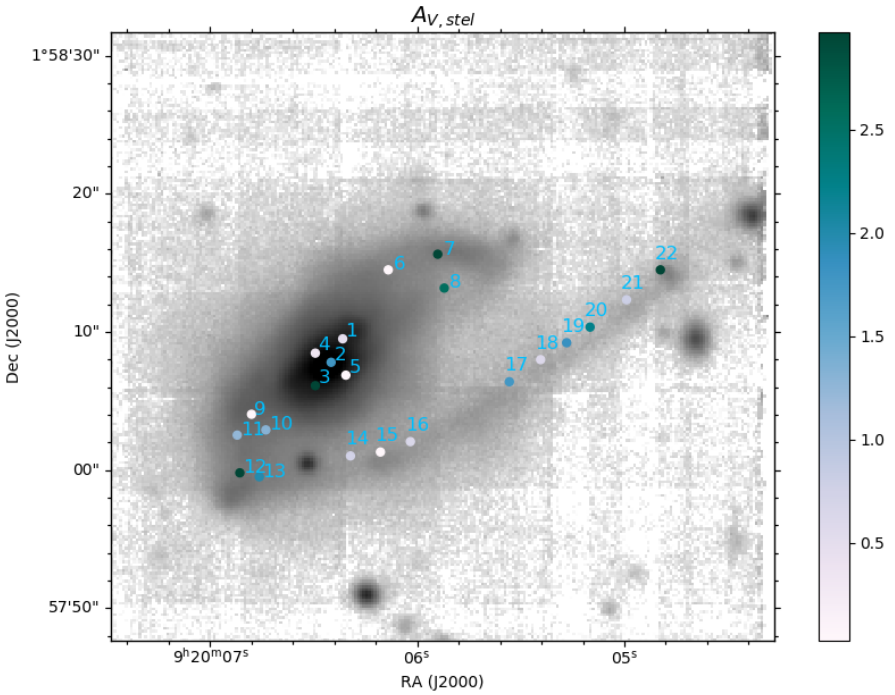

(a)

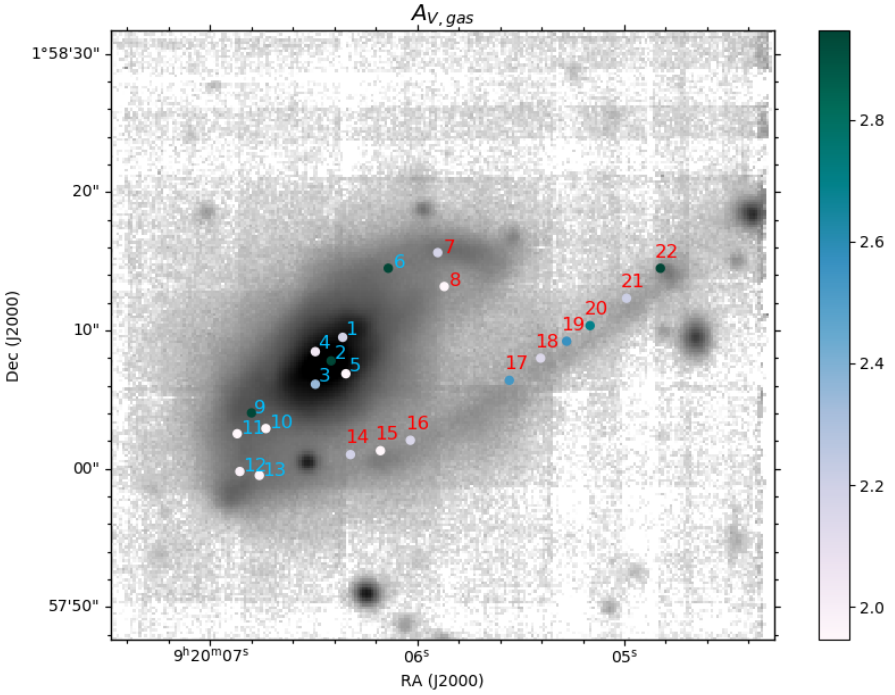

(b)

Figure 4.2: Comparison between (a) $A_{V,stel}$ and (b)$A_{V,gas}$. The values for the regions which are numbered in red corresponds to those obtained with a first degree polynomial fit. The colour bar indicates the attenuation value for each region.

4.3 Extinction corrected relative fluxes

Line emission fluxes are typically reported as relative to Hβ. Since we could not measure this line in some of the apertures, in this work we will present relative line fluxes relative to Hα, in the form $f(\lambda)/f(H\alpha)$.

Region	f($H\beta\lambda$4861)/f($H\alpha$)	f([O III]λ5007)/f($H\alpha$)	f([N II]λ6584)/f($H\alpha$)	f([S II]λ6716)/f($H\alpha$)	f([S II]λ6731)/f($H\alpha$)
1	0.299 ± 0.027	0.663 ± 0.047	0.807 ± 0.036	0.260 ± 0.240	0.169 ± 0.180
2	0.264 ± 0.025	0.770 ± 0.047	0.555 ± 0.060	0.194 ± 0.123	0.160 ± 0.109
3	0.291 ± 0.018	0.289 ± 0.023	0.510 ± 0.029	0.171 ± 0.143	0.234 ± 0.225
4	0.306 ± 0.033	0.566 ± 0.042	0.649 ± 0.031	0.231 ± 0.226	0.273 ± 0.288
5	0.311 ± 0.048	0.864 ± 0.082	0.765 ± 0.054	0.235 ± 0.332	0.188 ± 0.225
6	0.304 ± 0.304	-	0.432 ± 0.135	-	-
7	-	-	0.372 ± 0.234	0.389 ± 2.225	0.427 ± 1.803
8	-	-	1.228 ± 0.609	-	
9	-	-	1.324 ± 0.383	-	-
10	-	0.097 ± 0.116	0.651 ± 0.215	0.629 ± 1.525	0.809 ± 1.479
11	-	2.171 ± 0.749	3.679 ± 4.709	-	-
12	-	1.721 ± 0.681	3.678 ± 3.148	1.394 ± 4.246	1.200 ± 3.949
13	-	-	0.469 ± 0.093	0.162 ± 0.660	0.173 ± 0.498
14	-	-	1.193 ± 1.434	0.198 ± 5.362	0.197 ± 3.363
15	-	1.562 ± 0.444	1.021 ± 0.349	-	-
16	-	-	1.227 ± 0.962	-	-
17	-	14.481 ± 7.122	1.732 ± 1.319	2.207 ± 15.373	2.141 ± 14.490
18	-	-	0.489 ± 0.271	0.165 ± 1.723	0.165 ± 2.006
19	-	-	0.213 ± 0.328	1.540 ± 6.845	1.533 ± 6.308
20	-	1.347 ± 0.746	1.067 ± 0.825	-	-
21	-	0.355 ± 0.084	0.270 ± 0.085	-	-
22	-	0.062 ± 0.060	0.156 ± 0.051	0.303 ± 0.718	0.236 ± 0.472

Table 4.2: Integrated fluxes and errors for the emission lines used in this work.

The results in Table 4.2 consist of the corrected fluxes, which were obtained as explained in Sec 4.2. The uncertainties were estimated applying propagation of error, which includes Equation 3.2 and the error in the correction. Since PyNeb does not provide the latter error, we used a Montecarlo simulation to determine it.

E+A galaxies do not show any signs of on-going star formation. However, for the galaxy studied in this work, we found emission lines related to ionized gas. This is manifested in the results provided in Table 4.2. Considering that the overall ionization of gas seems to be stronger, particularly for Hα, in the nucleus of the galaxy (regions from 1 to 5, see Figure 3.1), one could wonder if this is the effect of an active galactic nucleus (e.d. a Seyfert galaxy in this particular case). The mechanism that explains ionized emission fluxes will be discussed in more detail in Section 4.4.

In the right sub-panel of Figure 3.2 it is clear that the modelled spectrum that FADO provides (the blue spectrum in the figure) does not adequately fit the Hβ absorption line. That issue was found for all regions and emerges as a consecuence of the strong absorption that the spectra present in Hβ: it is too strong for FADO to model it and this affects the obtained stellar model (and therefore, the gas spectrum). In order to calculate the integrated flux, we had to add an additional absorption component when building the Gaussian model for this particular line. In accordance with the spectral characteristics of E+A galaxies explained in Section 1.1, this behaviour reinforces SDSS J092006.44+ 015807.7's post-starburst status.

On another note, the reported fluxes for [S II]$\lambda\lambda 6716, 31$ are particularly tentative, since the

errors for both lines are rather high. They need further confirmation by means of e. g. bigger apertures to reduce the S/N ratio. However, the results are encouraging, seeing the agreement in the classification of the regions by means of the two used BPT diagrams (see Section4.4).

4.4 BPT diagrams

The BPT diagrams built for some regions are shown in Figure 4.3. The results are bound to the emission line fluxes that could be calculated in Section 4.3. The expected behaviour for the observed fluxes is as follows: even though the lines used in the BPT diagrams are chosen so as to minimize the amount of reddening between them, the lines that appear on the denominator of the logarithms present a slightly higher flux when corrected for attenuation (in this case, Hβ and Hα) since a smaller wavelength is associated with them. When the fluxes are corrected, it is expected that both values on the BPT axes become more negative, so the new, corrected values fall to the left and down the diagram.

For galaxies that present typical to moderate attenuation the effect explained in the previous paragraph is negligible. In fact, the difference in ratios of corrected and non-corrected fluxes is not noticeable in a BPT diagram. However, we have displayed in Section 4.2 the high attenuation values present in SDSS J092006.43+015807.7, so the correction is clearly discernible in Figure 4.3.

The regions that represent the nucleus of the galaxy fall in the AGN/Seyfert part of the diagrams. This suggests an AGN as a ionizing source, more than star formation. Region 3 is classified in the HII area of both BPTs. This does not necessarily mean that there is star formation going on there. Shields & Kennicutt (1996) discussed that sometimes HII regions are "hiding" weak AGNs or even shocks from supernova remnants, but it has not been established how common this "missclassification" is. Either way, the theoretical limits between AGN/Seyfert and HII regions are orientative demarcations, since other ionization mechanisms can be at play. In that sense, the optical data studied in this work should be discussed with extensive observations at radio, ultraviolet and/or X-ray wavelenghts. Also, Seyferts can be classified as low luminosity AGNs and they are usually found in spiral galaxies. Since SDSS J092006.43+015807.7 shows morphological signs of being the result of a merger, the nuclear data in Figure 4.3 is also coherent with the AGN classification. Seeing that there is only one region in the nucleus that is classified into the much-disputed HII region, it will be considered that the nucleus is formed by an AGN/Seyfert.

The data for both tidal tails, as represented in the BPT diagrams, is tentative because not all the apertures that we selected to map these structures could be displayed in Figure 4.3. The ones where the pertinent fluxes could be measured fall mostly in the HII region category. Region 15, in the [N II]λ6584 diagram are located near the theoretical limit but this can be explained as in the previous paragraph.

Region	$log([O\,\text{III}]\lambda5007/H\beta)$	$log([O\,\text{III}]\lambda5007/H\beta)_{corr}$	$log([N\,\text{II}]\lambda6584/H\alpha)$	$log([N\,\text{II}]\lambda6584/H\alpha)_{corr}$	$log([S\,\text{II}]\lambda\lambda6716,30/H\alpha)$	$log([S\,\text{II}]\lambda\lambda6716,30/H\alpha)$
1	0.899 ± 0.083	0.796 ± 0.159	-0.206 ± 0.025	-0.213 ± 0.051	-0.788 ± 0.056	-0.851 ± 1.052
2	1.259 ± 0.086	1.072 ± 0.192	-0.575 ± 0.055	-0.589 ± 0.117	-0.931 ± 0.050	-1.046 ± 0.831
3	0.112 ± 0.074	-0.010 ± 0.110	-0.663 ± 0.029	-0.673 ± 0.061	-0.835 ± 0.044	-0.910 ± 0.807
4	0.702 ± 0.092	0.615 ± 0.182	-0.426 ± 0.026	-0.433 ± 0.057	-0.636 ± 0.044	-0.690 ± 1.046
5	1.099 ± 0.116	1.022 ± 0.272	-0.261 ± 0.040	-0.267 ± 0.085	-0.816 ± 0.076	-0.863 ± 1.500
10	-2.230 ± 0.632	-2.317 ± 1.425	-0.423 ± 0.114	-0.439 ± 0.330	0.412 ± 0.127	0.363 ± 2.089
15	0.023 ± 0.210	-0.060 ± 0.536	-0.027 ± 0.133	0.021 ± 0.375	-	-
22	-2.302 ± 0.511	-2.350 ± 1.088	-1.847 ± 0.139	-1.856 ± 0.326	-0.567 ± 0.114	-0.627 ± 0.458

Table 4.3: Calculated values for the BPT diagrams, both for the non-corrected and corrected relative fluxes.

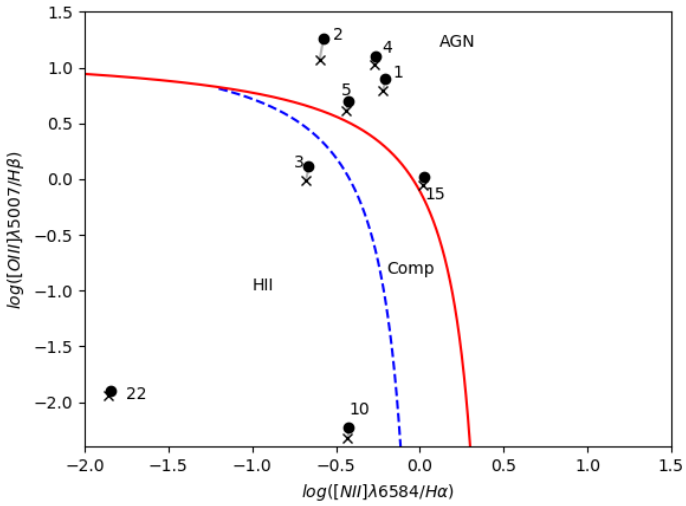

(a)

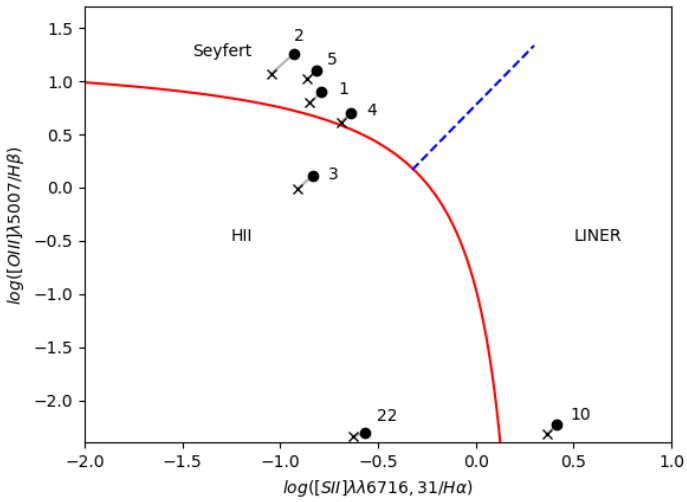

(b)

Figure 4.3: BPTs. The dots represent the logarithms of the pertinent fluxes before being corrected. The values represented by crosses have been corrected for attenuation. The red solid line and the blue dashed line represent the theoretical limits that separate the different mechanisms.

4.5 Sodium equivalent widths and attenuation

All of our apertures show an excess in the sodium doublet. Given the role of this doublet as a tracer of the amount of ISM, it is worth exploring the relation between the strength of these lines and attenuation. Equivalent widths for the Na D doublet were measured as described in Section 3.5 and the reported values can be found in Table 4.4. We found that these values are relatively high, ranging from 0.55 to 2.13 Å. An empirical law that correlates attenuation and strength of sodium lines can be found in Poznanski et al. (2012). Specifically:

$$log_{10}(E(B-V)) = 1.17 \times EW(D_1 + D_2) - 1.85 \tag{4.1}$$

where D1 and D2 stand for the Naλ5889 and Naλ5895 lines, respectively. This relation was derived using values for the total equivalent with $EW(D_1 + D_2) < 2$Å. This study is focused on a large sample of high-resolution and low-resolution spectra from the Milky Way taken from the SDSS. The authors provide a brief guide on how to use their findings to establish extinction and attenuation to extragalactic objects. Since we assumed the same extinction law for our calculations ($R_V = 3.1$) as on the aforementioned work, we propose a comparison between our study and theirs.

Region	EW(Naλ5889)	EW(Naλ5895)
1	1.504 ± 0.021	1.128 ± 0.021
2	2.131 ± 0.015	1.918 ± 0.015
3	1.918 ± 0.021	1.491 ± 0.021
4	1.587 ± 0.022	1.052 ± 0.024
5	1.451 ± 0.040	1.012 ± 0.040
6	1.278 ± 0.165	0.852 ± 0.165
8	1.429 ± 0.255	0.852 ± 0.242
9	1.372 ± 0.261	1.040 ± 0.291
11	0.564 ± 0.077	0.554 ± 0.082
12	0.836 ± 0.087	0.557 ± 0.040

Table 4.4: EW values for the Na$\lambda\lambda$5889, 95 doublet.

We compare the relation proposed by Poznanski et al. (2012) in Figure 4.4. The amount of sodium at a given attenuation for SDSS J092006.43+015807 exceeds the predicted values shown in the previous work. The behaviour is explained by the saturation of the Na D lines when they have individual EWs > 0.5Å. Furthermore, it is also remarked in Poznanski et al. (2012) that when the extinction source for a given region is not a diffuse interstellar component, it is not possible to guarantee that extinction will follow Equation (4.1).

As discussed, the origin of the Na$\lambda\lambda$5889, 95 absorption seems interstellar, as the modelling by FADO takes into account the stellar populations and this absorption feature is not adequate in the model. However, the analysis of the composition and physics of ISM is rather complex and far from the reach of this work. In addition, there are no available studies on the distribution of interstellar sodium for E+A galaxies so the consequent discussion of our results is tentative.

One of the hypothesis that could explain the distinct Na$\lambda\lambda$5889, 95 absorption features for SDSS J092006.43+015807.7 is the presence of dense, irregular dust regions both within the galaxy and line-of-sight. Another appealing theory can be found in Alatalo et al. (2016). This work is part of the Shocked POststarburst Galaxy Survey (SPOGS[1]) and its aim is to identify

[1] http://www.spogs.org/

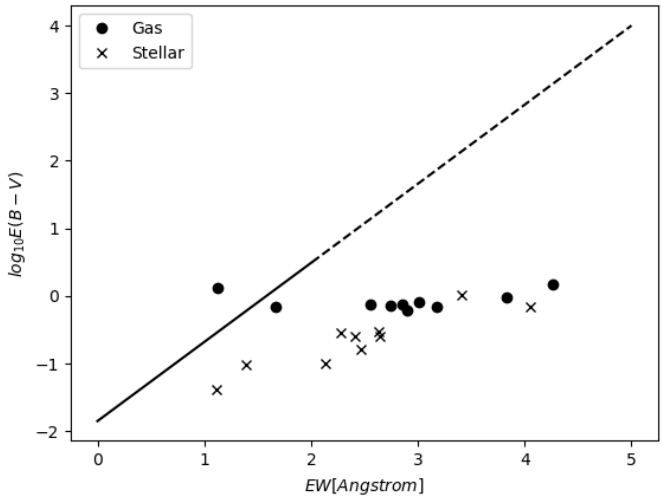

Figure 4.4: Relation between $E(B-V)$ and $EW(D_1+D_2)$. We present $E(B-V)$ values for both gas (circles) and stars (crosses). The solid black line represents the range of data that was studied in Poznanski et al. (2012); since our values exceed this range, we distinguished our particular span with the dashed line.

transforming galaxies in which nebular emission lines are excited via shocks instead of star formation mechanisms. In the cited work, they found that these type of galaxies present enhanced interstelar Na$\lambda\lambda$5889, 95 absorption features. The origin of these components could be traced to galaxy winds produced by shocks. However, it is also stated that AGNs (in particular, low-luminosity AGNs) could mimic the effects of shock-induced winds. Given this, one may wonder whether the excess in sodium that we detected could be associated with the presence of neutral gas in galactic winds caused by the AGN that we assume is located in the nucleus of the studied galaxy. This hypothesis could be tested with a detailed 2D kinematic study of this component of the ISM, well beyond the scope of this work.

4.6 Relative velocities

We calculated the velocities for the selected apertures as described in Section 3.7. In Figure 4.5 we represent the velocities of the gas relative to the innermost aperture; that is, Region 2 in Figure 3.1. We found that the velocity for that region is 25564 km s^{-1}, which is consistent with the NED value provided in Table 1.1. The results suggest that the smaller tidal tail (located to the north-west of the galactic nucleus) is approaching the viewer (negative relative velocities) and that south-east region is receding (positive relative velocities). Note that the larger tidal tail shows a gradient of velocities, with receding velocities to the south that become more positive towards the northern-most section. There is a difference of $\sim$ 500 km/s between the higher approaching and the higher (in absolute terms) receding velocities. In the same figure, we also present the relative velocities for the stellar populations calculated by FADO. The rotation appears to be practically the same, even though some specific regions do not follow it (particularly for the end of the larger tidal tail). The difference between the absolute maximum values for the approaching and receding apertures is $\sim$ 1000 km/s. However, these results are tentative since we have not dwelled on the analysis of the stellar populations.

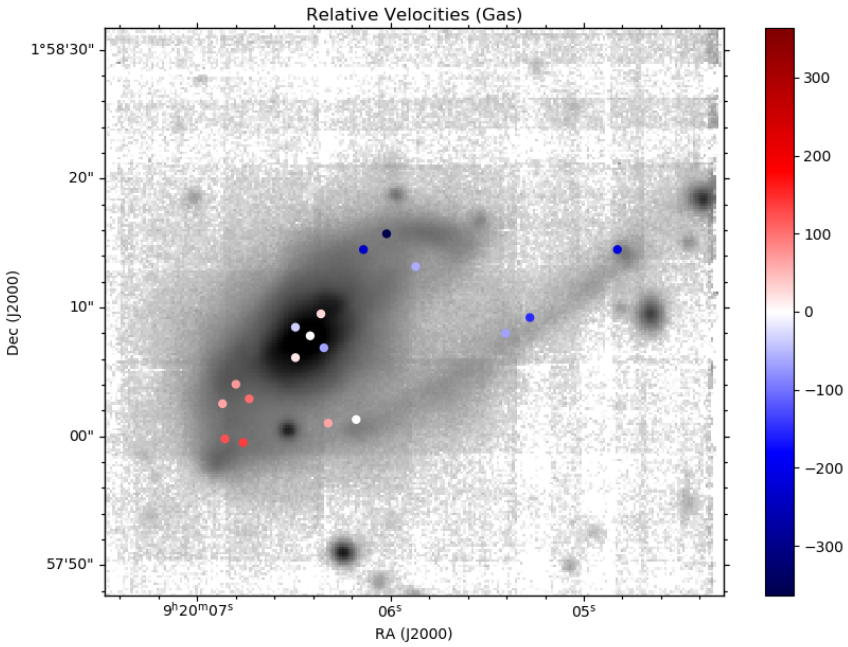

(a)

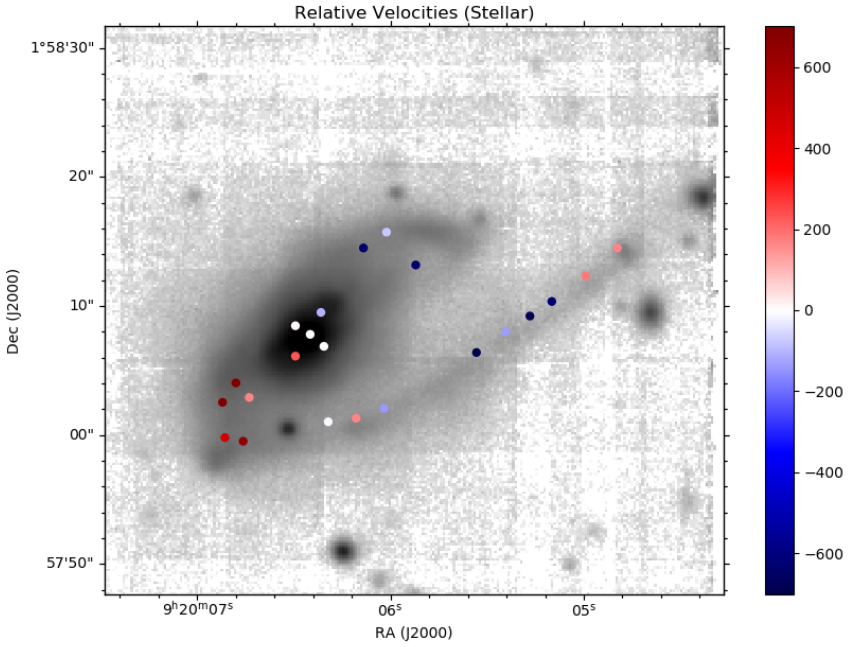

(b)

Figure 4.5: (a) Gas velocities relative to the innermost aperture of the nucleus (Region 2) and (b) Stellar velocities relative to the innermost aperture of the nucleus (Region 2). The values in the colour bar are in km/s. The positive ones are coloured in red, meaning that they are receding. The negative ones are coloured in blue: that is, they are approaching.

Norton et al. (2001) were the first to study the spatially-resolved kinematic of the stellar populations in E+A galaxies. They obtained a sample of 21 long-slit spectra of E+As in order to study the distribution of rotation within the galaxies. This pioneer work concluded that E+A could constitute rapidly or slowly rotating systems, or show no rotation at all. In fact, they determined that about 70% presented no signs of rotation. Multiple observations and numerical simulations regarding the kinematics of E+As have been done since Norton et al. (2001) published their results, but all of them seek to establish a relation between the age of stellar populations and the dynamical features of the galaxies (e. g. Pracy et al. (2009)). However, these studies can also aid to clarify the origin of E+As. We are going to focus on this last point for this work. As a side note, FADO gives predictions regarding the ages of stellar populations but in this study we have only used the code as a tool to separate the stellar and ISM information.

Numerical simulations by Bekki et al. (2005) give evidence on physical properties for E+A galaxies. Particularly, they study the kinematics of these galaxies based on the merger origin hypothesis. The factor that determines the stellar motions is the mass of the merger: for an equal-mass merger, the resulting system should be dynamically pressure supported; for an unequal one and tidal interactions, rotation of the young stellar populations is expected. These results have been confirmed by spatially resolved spectroscopic observations by Pracy et al. (2009), among others. Our reported velocities, with large differences between the approaching and receding sides of the galaxy, suggest an unequal mass merger as a possible scenario for its origin.

Chapter 5

Conclusions and future work

Resumen. *En este último apartado del trabajo, reunimos las discusiones de los resultados. En cuanto al origen de SDSS J092006.43+015807.7, hemos concluido que se formó debido a un merger entre dos galaxias con masas diferentes. Esto viene fundamentado por la propia morfología de la galaxia y el tipo de rotación que presenta. A partir del análisis de los diagramas BPT, asumimos que el nucleo de la galaxia está constituido por un AGN que, a su vez, podría ser el causante de la terminación de formación estelar. El análisis de la atenuación y su influencia en las líneas de emisión indican que hay una cantidad considerable de gas ionizado en la galaxia. De forma complementaria, el exceso de sodio indica que hay más contribución del medio interstellar, aparte de las gas ionizado. Para terminar, ponemos en contexto nuevas líneas de trabajo para el futuro, con el fin de mejorar y ampliar los conocimientos sobre esta galaxia y sobre las E+A en general.*

The analysis of a series of representative apertures for SDSS J092006.43+015807.7 and their respective spectra have given us the necessary data to make a first approach into this galaxy's characteristics. Not only have we studied its spectral properties, but we also derived parameters that allowed us to discuss the rarities of this galaxy. E+As galaxies are elusive and research on them is not as extensive as for others, but we hope to contribute to this field with the following results:

(i) SDSS J092006.43+015807.7 presents a distinctive bulge-dominated, disturbed morphology. This is consistent with other E+A galaxies that have been classified and studied, and the presence of tidal tails strengthens the hypothesis of a merger origin. It has been established (see Baron et al. (2018)) that AGN-driven winds could strip a galaxy from its gas, thus quenching star formation within. The study of the spectral properties of the internal region of the selected galaxy suggests that an AGN dominates the ionization in the nucleus of the galaxy.

(ii) SDSS J092006.43+015807.7 presents the spectral properties that are expected for a post-starbust galaxy: that is, strong Balmer absorption lines, and even if the [O II] line is detected in the SLOAN spectrum, it is relatively faint. In particular, the apertures in the central region present such strong absorption Balmer lines that the adopted population synthesis tool (FADO) could not adequately model it. In order to extract the information of the ionized gas associated to the aforementioned apertures, we added an additional absorption component when measuring the integrated flux associated with Hβ.

(iii) Gas ($A_{V,gas}$) and stellar ($A_{V,stel}$) attenuation is stronger in the nuclear region of the galaxy.

There is no further discernible pattern on how this values vary within the galaxy, since both tidal tails present similar attenuation with no perceptible dependence on galactocentric radius. We compared the calculated attenuation for both gas and stars to typical data for star-forming and spiral galaxies, finding a similar $A_{V,stel}/A_{V,gas}$ as in those types of galaxies. To our knowledge, the analysis of the $A_{V,stel}/A_{V,gas}$ ratio using spatially resolved measurements presented in this work is unique for an E+A galaxy.

(iv) The presence of emission lines in the spectra of the studied regions proves that there is a substantial amount of ionized gas in the galaxy. The correction of the relative fluxes of said lines gives insight on the source of ionization. The subsequent BPT diagrams indicate that the source of ionization is an AGN.

(v) We determined a considerable amount of interstellar Na D, indicating the presence of a substantial amount of ISM beyond the ionized gas mentioned in the previous conclusion. The range of EWs measured for the doublet ranges between 0.554 and 2.131Å. For this set of values, the Na D does not trace extinction, as the relation clearly saturates for values above 0.5 Å.

(vi) The rudimentary analysis of the kinematics of SDSS J092006.43+015807.7 seems to favour the rotational support of the galaxy. The results suggest that the smaller tidal tail (located to the north-west of the galactic nucleus) is approaching the viewer (negative relative velocities) and that south-east region is receding (positive relative velocities).We found differences of ∼500 km/s between the maximum approaching and receding (in absolute terms) velocities for the studied apertures. All this suggests that SDSS J092006.43+015807.7 is the result of an unequal mass merger.

All in all, we conclude from its morphology and rotation, that SDSS J092006.43+015807.7 was formed in a merger of two unequal mass galaxies. Presumably, it contains an AGN in its center, which could be the source of the abruptly-quenched star formation. The presence of ionized gas (well founded on the existence of emission lines) suggests that the most-recently formed stars could still be embedded in their molecular birth clouds. Also, ISM in general is abundant within the galaxy, as the excess of the sodium doublet indicates. Its E+A status is reinforced by the strong Balmer absorption lines that we found and its subsequent modeling, which had to be aid with an additional absorption component.

5.1 Future work

In this work, we present a preliminary study of SDSS J092006.43+015807.7. Due to computational limitations, it has been restricted to the analysis a series of representative apertures. However, this study sets a starting point for the deciphering of this galaxy's characteristics. First of all, a similar study but with larger apertures should be done. This would improve the S/N ratio and the results should be compared for both works, specially for those values that present high errors: for example, the relative flux of [S II]$\lambda\lambda$6717,31 with respect to Hα (see Table 4.2). Determining the behaviour of the gas and stellar attenuation for all the galaxy could also benefit for data with an improved S/N ratio, given that we had to estimate the gas attenuation values for the majority of the apertures (in particular, for those located in the tidal tails).

On another note, given all the data and results that we gathered in this work, it would be convenient to map the stellar populations for all the apertures that we selected. The description of the stellar component of the galaxy would complement all the results that we have come

across in this work, given that it could aid, for example, in the determination of the reach of the post-starbust region: that is, whether it is centralised or not. The dynamical features of E+A galaxies seems to be associated with the age of the stellar populations, so our elemental analysis of the studied galaxy's rotation should also benefit from this extended line of work.

Appendix A

FADO plot for Region 1

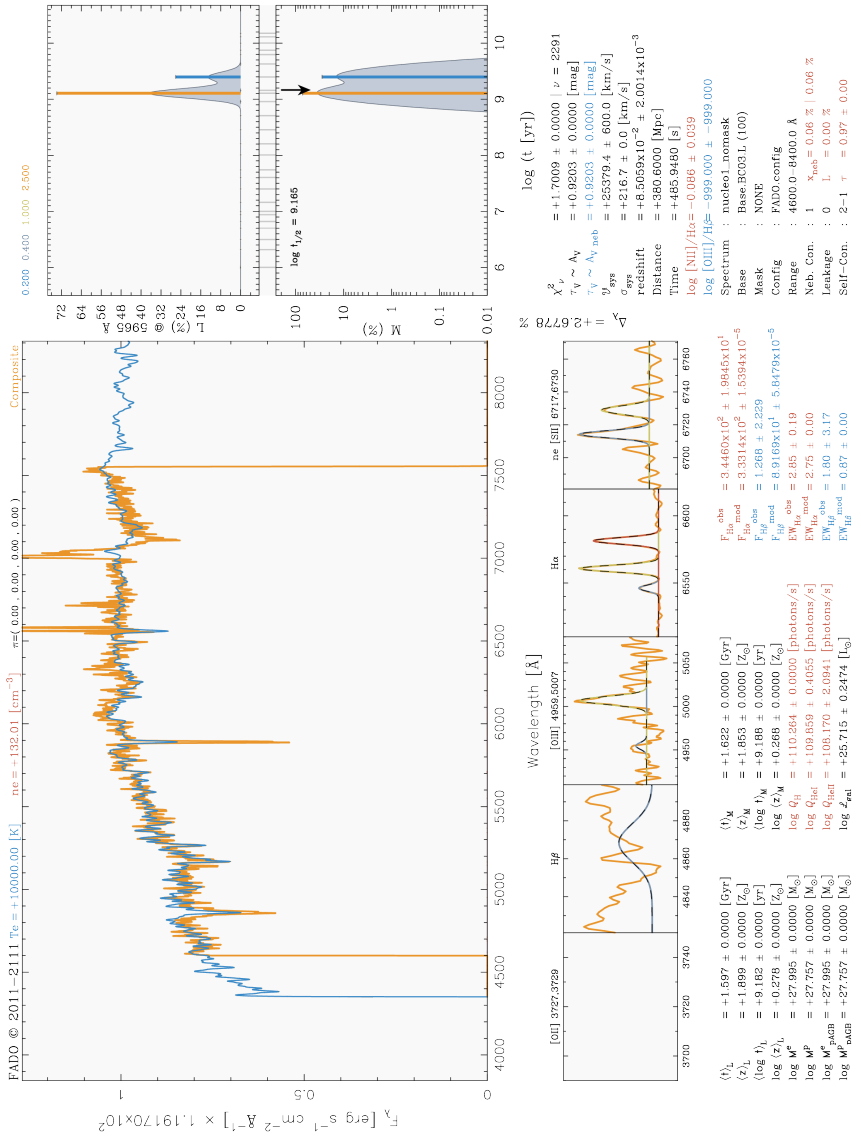

Figure A.1: FADO plot for Region 1

In Figure A.1 we present a standard plot given by FADO as part of the output when modelling spectra. In particular, the one we show corresponds to Region 1, which is the one that we have been referring to in the models in Section 3. In this image, the dominant panel shows the comparison between the observed spectrum (in orange) and the model (in blue). The subpanels below the main plot present zooms at a specific spectral range. It is notable that FADO fails to model Hβ, which is represented in the second subpanel. This graphic output also contains some interesting parameters estimated by FADO. For our work, we have used A_V in Section 4.2 and v_{sys} in Section 4.6.

Bibliography

Aguado, D. S., Ahumada, R., Almeida, A., et al. 2018, The Fifteenth Data Release of the Sloan Digital Sky Surveys: First Release of MaNGA Derived Quantities, Data Visualization Tools and Stellar Library

Ahn, C. P., Alexandroff, R., Allende Prieto, C., et al. 2012, ApJS, 203, 21

Ahn, C. P. & et al. 2013, VizieR Online Data Catalog, V/139

Alatalo, K., Cales, S. L., Rich, J. A., et al. 2016, ApJS, 224, 38

Astropy Collaboration, Robitaille, T. P., Tollerud, E. J., et al. 2013, A&A, 558, A33

Baldwin, J. A., Phillips, M. M., & Terlevich, R. 1981, PASP, 93, 5

Baron, D., Netzer, H., Prochaska, J. X., et al. 2018, MNRAS, 480, 3993

Baron, D. & Poznanski, D. 2017, MNRAS, 465, 4530

Bekki, K., Couch, W. J., Shioya, Y., & Vazdekis, A. 2005, MNRAS, 359, 949

Calzetti, D., Armus, L., Bohlin, R. C., et al. 2000, ApJ, 533, 682

Cardelli, J. A., Clayton, G. C., & Mathis, J. S. 1989, ApJ, 345, 245

Castellanos, M., Díaz, A. I., & Terlevich, E. 2002, MNRAS, 329, 315

Dressler, A. & Gunn, J. E. 1983, ApJ, 270, 7

Gaia Collaboration. 2018, VizieR Online Data Catalog, I/345

Gomes, J. M. & Papaderos, P. 2017, A&A, 603, A63

Goto, T. 2005, MNRAS, 357, 937

Goto, T. 2007, MNRAS, 381, 187–193

Goto, T., Yagi, M., & Yamauchi, C. 2008, MNRAS, 391, 700

Greener, M. J., Aragón-Salamanca, A., Merrifield, M. R., et al. 2020, MNRAS [[arXiv]2005.02772]

Kewley, L. J., Groves, B., Kauffmann, G., & Heckman, T. 2006, MNRAS, 372, 961

Luridiana, V., Morisset, C., & Shaw, R. A. 2015, A&A, 573, A42

Norton, S. A., Gebhardt, K., Zabludoff, A. I., & Zaritsky, D. 2001, ApJ, 557, 150

Osterbrock & Ferland. 2005, Astrophysics of Gaseous Nebulae and Active Galactic Nuclei, 2nd edn. (University Science Books)

Pascucci, I., Edwards, S., Heyer, M., et al. 2015, ApJ, 814, 14

Poznanski, D., Prochaska, J. X., & Bloom, J. S. 2012, MNRAS, 426, 1465

Pracy, M., Kuntschner, H., Couch, W., et al. 2009, MNRAS, 396, 1349

Price-Whelan, A. M., Sipőcz, B. M., Günther, H. M., et al. 2018, AJ, 156, 123

Rieke, G. H. & Lebofsky, M. J. 1985, ApJ, 288, 4

Schlafly, E. F. & Finkbeiner, D. P. 2011, ApJ, 737, 103

Shields, C. & Kennicutt, R. C., J. 1996, in Astronomical Society of the Pacific Conference Series, Vol. 103, The Physics of Liners in View of Recent Observations, ed. M. Eracleous, A. Koratkar, C. Leitherer, & L. Ho, 217

Skrutskie, M. F., Cutri, R. M., Stiening, R., et al. 2006, AJ, 131, 1163

Weilbacher, P. M., Palsa, R., Streicher, O., et al. 2020, arXiv e-prints, arXiv:2006.08638